Article | Received 9 June 2024; Accepted 11 December 2024; Published 3 January 2025
https://doi.org/10.55092/am20250001

Transfer learning-enhanced physics informed neural network for accurate melt pool prediction in laser melting

Qingyun Zhu[1], Zhengxin Lu[1], and Yaowu Hu[1,2,*]

[1] The Institute of Technological Sciences, Wuhan University, 430072 Wuhan, China
[2] School of Power and Mechanical Engineering, Wuhan University, 430072 Wuhan, China

* Correspondence author; E-mail: yaowuhu@whu.edu.cn.

Highlights:

- A novel transfer learning-enhanced PINN method is proposed.
- This method can predict the melt pool morphology in selective laser melting.
- This method exhibits higher efficiency than conventional PINN and simulation methods.
- The performance of this method is superior to mainstream data-driven methods.

Abstract: The profile of the melt pool is essential in selective laser melting (SLM) to control the process quality and avoid defects. Physics informed neural network (PINN) method is proposed to address challenges in various science and engineering problems when traditional numerical calculations are time-consuming, or deep learning (DL) methods have high demand for data. However, SLM process involves many complex physical phenomena. Low-fidelity data from low-fidelity models struggle to accurately reflect these phenomena, while high-fidelity data from high-fidelity models contains more physical equations, making it difficult for current PINN. This article proposed a transfer learning-enhanced PINN (TLE-PINN) method using high-fidelity data for precise and fast melt pool prediction. It contains the enhanced PINN (EPINN) and transfer learning framework. The EPINN model integrates the heat transfer law and boundary condition to loss function, imposing strong physical constraints on data. Then, the transfer learning framework, combining the concepts of PINN and DL, initially trains with PINN and then further fine-tunes it using DL method. Notably, it only uses a single model, which is more convenient to traditional methods that require two models. The developed solution demonstrates outstanding performance when compared with experiments and existing methods, showing significant potential for industrial applications.

Keywords: selective laser melting; melt pool; deep learning; PINN; transfer learning

1. Introduction

With the rapid advancement of laser manufacturing technology, selective laser melting (SLM) has emerged as an advanced surface processing method. SLM offers several advantages in manufacturing metal components and enhancing surfaces, including high precision, efficiency, minimal heat-affected zones, and energy savings [1]. SLM is extensively utilized in the automotive, aerospace, and other industries [2]. Notably, the size of the melt pool and the distribution of temperature are pivotal factors influencing sample quality, performance, and processing efficiency in SLM [3]. Additionally, various coating functions, such as corrosion and wear resistance, can be achieved by controlling the melt pool size. Therefore, research on melt pools in the SLM process is particularly important.

SLM is a multi-scale, multi-physics process. Numerical analysis, a well-established method, is used to predict melt pool formation and properties through mathematical modeling [4,5]. For example, Ping *et al.* developed a multi-physics model to investigate the solidification process during the laser welding of 5083 aluminum alloy [6]. Qing *et al.* developed a multi-scale model that integrates conductive heat transfer and dendritic solidification to simulate the fused deposition process in 3D printing [7]. However, traditional numerical methods require considerable time and high-performance computing frameworks to solve complex multi-scale, multi-physics models, which cannot meet industrial demands.

With advancements in artificial intelligence, deep learning (DL) methods have become widely utilized in industrial applications[8,9]. Notably, physics-informed neural networks (PINNs), which incorporate physical laws into the loss function, exhibit superior performance in science and engineering [10–14]. For instance, Seid *et al.* applied PINN models to solve the heat conduction equation and provided a novel computational framework that can reliably and quickly predict results after adequate training [15]. Li *et al.* developed a PINN model that predicts the temperature field during the laser metal deposition process without requiring labeled data [16]. Wang *et al.* proposed a physics-informed machine learning method that connects related parameters in selective laser melting to effectively predict quality characteristics [17]. Akbari *et al.* developed a physics-aware machine learning method to predict melt pool shape and geometry in metal additive manufacturing [3]. Hosseini *et al.* use PINNs for thermal analysis in laser powder bed fusion [18]. Jagtap *et al.* [19] introduces adaptive activation functions for PINNs, enhancing the approximation of smooth and discontinuous functions as well as solutions to nonlinear partial differential equations.

Although the aforementioned methods contribute to solving certain simulation models, most PINN methods, due to their simplistic structure, exhibit unacceptable performance when dealing with industrial applications that involve complex physical information, such as laser processing. For example, Jiang [20] proposed the PINN method for predicting the melt pool morphology performs well with low-turbulence effect cases while performing poorly with high-turbulence effect cases. Zhu [21] proposed the PINN method for predicting the melt pool morphology performs in high-turbulence effect cases, and its train speed and efficiency can be further improved. Therefore, further improvements are needed.

With the rise of transfer learning techniques, these methods have been applied in various fields (e.g., computer vision [22], fault diagnosis [23], and deep natural language processing [24]). Transfer learning methods can enhance the adaptability and robustness of models by utilizing different types of data or models, such as fine-tuning pre-trained models or using existing features for training [25].

In light of the above discussion, this article proposes a transfer learning-enhanced PINN (TLE-PINN) method for training high-fidelity data. It incorporates an enhanced PINN (EPINN) model and a transfer learning framework to achieve accurate melt pool prediction in SLM. The primary innovations and methodologies of this study are as follows:

(1) EPINN model. The EPINN model incorporates heat transfer laws and boundary conditions, including the laser-activated surface and other insulating surfaces, into the loss function, providing strong physical constraints on the data. Additionally, a locally adaptive activation function is applied to the network to enhance convergence performance during the training process.

(2) Transfer learning framework. The proposed transfer learning framework combines concepts from both PINN and DL methods. Notably, unlike traditional transfer learning methods that use two models for parameter transfer, the proposed framework employs only a single model for implementation. Specifically, the PINN model is first trained using high-fidelity data, and then the last layer parameters are updated using DL methods while keeping the other layer parameters frozen. The proposed method effectively trains high-fidelity data, enhances training speed, and prevents overfitting during the training process.

(3) Experimental validation. To validate the effectiveness of the TLE-PINN method, SLM experiments with laser scanning speeds of 1–9 mm/s were conducted, and the corresponding melt pool profiles were obtained for validation. Meanwhile, related methods such as PINN and data-driven approaches were also applied and compared to the proposed method across different aspects. Additionally, to validate the effectiveness of the high-fidelity model, a low-fidelity model is established for comparison. The developed solution demonstrates superior performance compared to existing methods and shows significant potential for industrial applications.

2. Mathematical modeling

2.1. Governing equations

During the SLM process, laser energy is applied to the upper surface of the sample, causing localized heating and melting of the surface. Subsequently, fluid flow driven by surface tension is induced. The governing equations of the high-fidelity model incorporate heat transfer, fluid flow, and mass exchange between different phases. The conservation equations for mass, momentum, thermal energy, and solute transport are defined as follows:

$$\frac{\partial \rho}{\partial t}+\frac{\partial(\rho u_i)}{\partial x_i}=0 \tag{1}$$

$$\frac{\partial(\rho u_i)}{\partial t}+\frac{\partial(\rho u_i u_j)}{\partial x_i}=\frac{\partial}{\partial x_i}[(\mu+\rho \nu_T)\frac{\partial u_j}{\partial x_i}]+S_{u_i} \tag{2}$$

$$\frac{\partial(\rho cT)}{\partial t}+\frac{\partial(u_i \rho cT)}{\partial x_i}=\frac{\partial}{\partial x_i}(K\frac{\partial T}{\partial x_i})+S_T \tag{3}$$

$$\frac{\partial(\rho C)}{\partial t}+\frac{\partial(\rho u_i C)}{\partial x_i}=\frac{\partial}{\partial x_i}(\rho D\frac{\partial C}{\partial x_i})+S_C \tag{4}$$

in which, ρ is the density of liquid metal (kg/m^3). u_i and u_j are the velocity field in direction i and j (i, j = 1,2,3) (m/s). μ is the dynamic viscosity of liquid metal (N·s/m^2). t is the time (s). x is the spatial coordinate (m). c is the specific heat capacity (J/(kg·K)). T is the temperature. K is the thermal

conductivity. D is the mass diffusion coefficient. S_{ui}, S_T, and S_C are the source terms in the conservation equations for momentum, thermal energy, and solute transport, respectively.

$$\begin{cases} S_{u_i} = -\dfrac{\partial p}{\partial x_i} + \dfrac{\partial}{\partial x_j}(\mu \dfrac{\partial u_j}{\partial x_i}) - K_0 \dfrac{(1-f_l)^2}{f_l^3 + B} u_i + \rho g_i \beta_T (T - T_{ref}) - V_{scan} \mu \dfrac{\partial \rho u_i}{\partial x_i} - V_{scan} \mu \dfrac{\partial \rho u_i}{\partial x_1} \\ S_T = -\dfrac{\partial(\rho \Delta H)}{\partial t} - \dfrac{\partial(\rho u_i \Delta H)}{\partial x_i} - V_{scan} \dfrac{\partial \rho c T}{\partial x_1} - V_{scan} \dfrac{\partial \rho \Delta H}{\partial x_1} \\ S_C = 0 \end{cases} \tag{5}$$

in which B is a very small positive number introduced to avoid division by zero. V_{scan} is the laser scanning speed. β_T and β_C are the volume expansion caused by temperature gradient and concentration gradient, respectively. Defining the liquid mass fraction as f_l

$$f_l = \begin{cases} 1, & T > T_l \\ \dfrac{T - T_s}{T_l - T_s}, & T_s \le T \le T_l \\ 0, & T < T_s \end{cases} \tag{6}$$

The individual physical quantities of the solid-liquid mixture in the melt pool are calculated according to the following equation

$$c = f_s c_s + f_l c_l \tag{7}$$

$$K = \left(\frac{g_s}{K_s} + \frac{g_l}{K_l} \right)^{-1} \tag{8}$$

To speed up the calculation and simplify the calculation process, the liquid phase density and solid phase density of 42CrMo are set equal. When the effect of turbulence in the melt pool is taken into account, the turbulent kinetic energy equation k and the turbulent dissipation rate equation ε can be written as Equation (9) and (10), respectively.

$$\frac{\partial(\rho k)}{\partial t} + \frac{\partial(\rho u_i k)}{\partial x_i} = \frac{\partial}{\partial x_i}[(\mu + \rho \frac{v_T}{\sigma_K}) \frac{\partial k}{\partial x_i}] + S_k \tag{9}$$

$$\frac{\partial(\rho \varepsilon)}{\partial t} + \frac{\partial(\rho u_i \varepsilon)}{\partial x_i} = \frac{\partial}{\partial x_i}[(\mu + \rho \frac{v_T}{\sigma_\varepsilon}) \frac{\partial \varepsilon}{\partial x_i}] + S_\varepsilon \tag{10}$$

in which ε and k are the turbulent dissipation rate and the turbulent kinetic energy. v_T is the eddy viscosity. σ_T is the energy Planck number. S_k and S_ε are the source term of turbulent energy equation and turbulent dissipation rate, which can be expressed as

$$\begin{cases} S_k = \rho P - \rho \varepsilon - \rho V_{scan} \dfrac{\partial k}{\partial x_1} \\ S_\varepsilon = C_{\varepsilon 1} \rho P \dfrac{\varepsilon}{k} - C_{\varepsilon 2} \rho \dfrac{\varepsilon^2}{k} - \rho V_{scan} \dfrac{\partial \varepsilon}{\partial x_1} \end{cases} \tag{11}$$

where $P = 2 v_T \overline{S}_{ij} \overline{S}_{ij}$. v_T is the eddy viscosity. $\overline{S}_{ij}$ is the average strain rate tensor.

2.2. Boundary conditions

The input energy, represented by the laser beam, can be approximated as an axisymmetric Gaussian distribution, which is expressed as follows:

$$q_{laser} = \frac{Q\eta}{\pi r_b^2} \exp\left(-\frac{x^2 + y^2}{r_b^2}\right) \tag{12}$$

in which Q is the laser power. r_b is the radius of the input laser beam. η is the laser absorption coefficient. Then, the heat loss due to convective heat transfer is described as

$$q_{loss} = h_c(T - T_e) + \sigma_b \varepsilon (T^4 - T^4) \tag{13}$$

where h_c is the thermal convection coefficient. σ_b is the Stefan-Boltzmann constant. T_e is the ambient temperature. Accordingly, the energy boundary condition at the sample's upper surface can be expressed as follows:

$$K\frac{dT}{dz} = q_{laser} - q_{loss} \tag{14}$$

The energy boundary condition for the remaining surfaces is natural convection. Given that the upper surface of the melt pool is assumed to be flat, the Marangoni convection boundary condition is expressed as follows:

$$\begin{cases} \mu\dfrac{du}{dz} = f_l \dfrac{\partial\gamma}{\partial T}\dfrac{\partial T}{\partial x} \\ \mu\dfrac{du}{dz} = f_l \dfrac{\partial\gamma}{\partial T}\dfrac{\partial T}{\partial y} \end{cases} \tag{15}$$

in which f_l is the liquid mass fraction. Related details can be seen in [20,26].

2.3. Developed simulation program

The 3D high-fidelity heat transfer models are developed using the finite volume method and implemented in FORTRAN, and their computed results are shown in Figure 1. The CW laser performs a single pass scan at a relatively slow speed along the x-axis on the upper surface of the sample according to Figure 1a,b. The melt pool morphology and heat affected zone can be seen in the cross-section of the sample according to Figure 1c. The simulation parameters utilized in this study are derived from [20,26], as presented in Table 1. These parameters were calibrated by the researchers and adjusted based on the consistency between the computed results and experimental data. The adjusted computational results are consistent with the experimental data and can be utilized as input data for the proposed algorithm. The simulation models discussed in this study are listed in Table 2, in which the high-fidelity model includes all governing and boundary equations outlined in Sections 2.1 and 2.2, while the low-fidelity model excludes those related to turbulence effects.

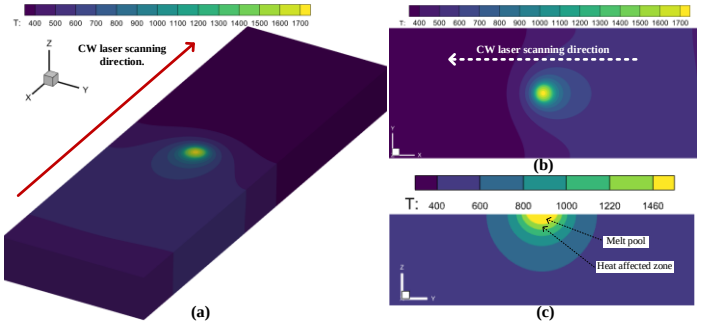

Figure 1. (a) 3D high-fidelity heat transfer model. **(b)** Temperature distribution in the surface of the sample. **(c)** Melt pool morphology and heat affected zone in the cross-section of the sample.

Table 1. Material and laser properties in this paper.

Parameter	Value
Thermal conductivity of solid	40.5 W(m·K)
Solidus temperature	1420 K
Specific heat of solid	470 J/(kg·K)
Thermal conductivity of liquid	22 W(m·K)
Liquidus temperature	1460 K
Specific heat of liquid	700 J/(kg·K)
Density	7800 kg/m^3
Emissivity	0.2
Effective radius of the laser	0.5 mm
Stefan-Boltzmann constant	5.67×10^{-8}
Ambient temperature	298 K

Table 2. The simulation models discussed in this article.

Low-fidelity model	3D heat transfer model without turbulence
High-fidelity model	3D heat transfer model with turbulence

3. Proposed algorithm

3.1. Input data

The EPINN architecture is illustrated in Figure 2a. The input data includes both temperature-unlabeled and temperature-labeled datasets. Specifically, the temperature-unlabeled data consist of experimental spatial coordinates (x, y, z) and laser scanning speed (v). These are used to fit the governing and boundary condition equations. Temperature-labeled data consist of (x, y, z, v) and the temperature (T), which are sampled from the high-fidelity model. These are utilized to solve the governing, boundary condition, and residual equations.

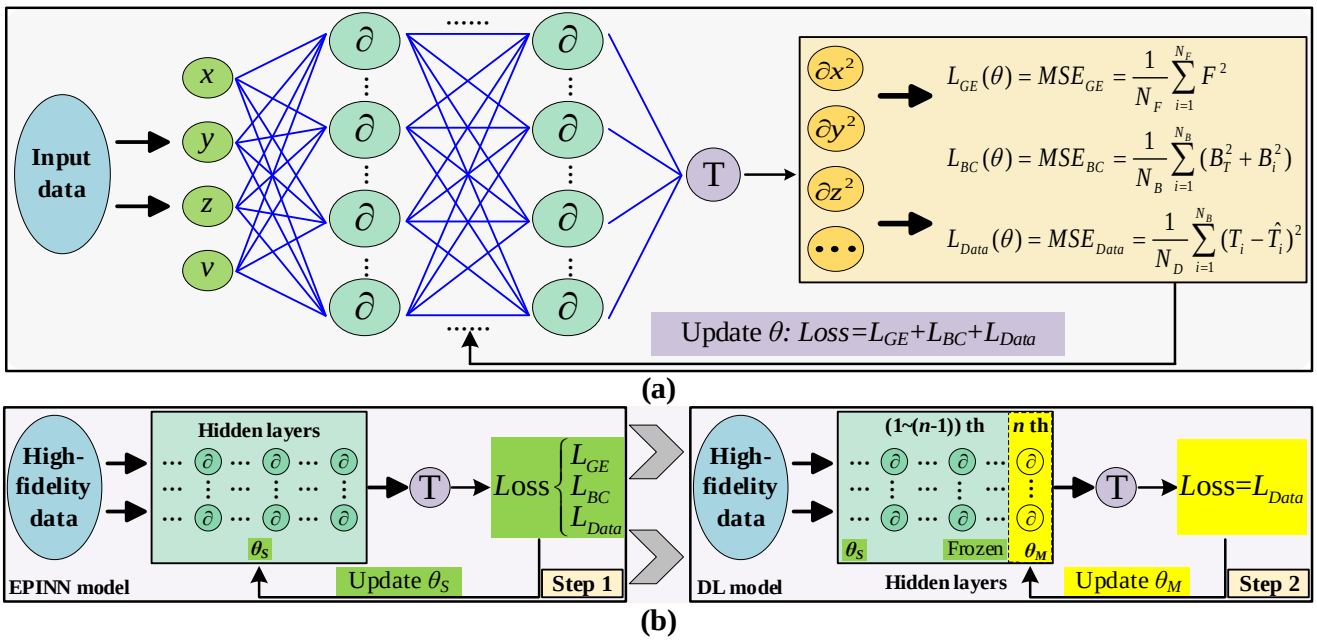

Figure 2. (a) Enhanced PINN architecture. **(b)** TLE-PINN framework.

3.2. Enhanced PINN

The EPINN model is designed to address the limitations of deep learning (DL) methods, which have a high demand for data, and conventional physics-informed neural networks (PINNs), which are inefficient and impose weak physical constraints. It is particularly effective for high-fidelity data that contains rich physical information. The EPINN model comprises five hidden layers, each with 100 neurons. The predicted temperature (T) serves as the output layer. During training, the Swish function is employed as the activation function, and automatic differentiation [27] is used to compute the differential terms. Specifically, the locally adaptive activation function [19,28] is applied to enhance the training speed and improve network convergence, which can be expressed as follows:

$$\sigma_n(a_n(w_n^T x_n + b_n)) \tag{16}$$

in which σ_n is the activation function. x_n is the input neurons. w_n and b_n are the weight and bias of neurons, respectively. a_i is the trainable hyper-parameter. Unlike in general networks where a_i=1, the slope of the original activation function in the EPINN model can be optimized by training a_n. This optimization enhances training quality. Additionally, w_n, b_n and a_n are updated using stochastic gradient descent, with optimization performed via the ADAM optimizer followed by L-BFGS. This process further improves network convergence.

The loss function, which incorporates physical laws to update network parameters during the back-propagation process, primarily consists of three components, as illustrated in the Figure 2a. First, the conservation of thermal energy as given in (3), and its residual equation F and mean squared error (MSE) loss L_{GE} are expressed as

$$\begin{cases} F = \dfrac{\partial}{\partial x_i}(K\dfrac{\partial T}{\partial x_i}) - \dfrac{\partial(\rho c T)}{\partial x_i} - V_{scan}\dfrac{\partial(\rho c T)}{\partial x_i} \\ L_{GE} = \dfrac{1}{N_F}\sum_{i=1}^{N_F} F^2 \end{cases} \tag{17}$$

Given that complex governing equations can complicate the training process, the heat transfer equation can be simplified by omitting the fluid flow term, as suggested in [20,26]. Second, the residual equation for the laser action surface boundary condition can be expressed as

$$B_T = K\frac{dT}{dz} - (q_{laser} - q_{loss}) \tag{18}$$

The residual equation for the boundary condition of the five insulating surfaces can be written as follows:

$$B_i = \frac{\partial T}{\partial n_i} \tag{19}$$

in which n_i is the outward normal direction on the boundary. Therefore, the MSE equation for the boundary condition can be expressed as follows:

$$L_{BC} = \frac{1}{N_B}\sum_{i=1}^{N_B}(B_T^2 + B_i^2) \tag{20}$$

Third, the residual equation between the predicted temperature T and the true temperature T is written as follows:

$$L_{Data} = \frac{1}{N_D}\sum_{i=1}^{N_D}(T_i - \hat{T})^2 \tag{21}$$

Consequently, the loss function can be expressed as follows:

$$L = \lambda_1 L_{GE} + \lambda_2 L_{BC} + \lambda_3 L_{Data} \tag{22}$$

where λ_1, λ_2, and λ_3 are the weights of L_{GE}, L_{BC}, L_{Data}, respectively. The main improvements of the EPINN are as follows: 1) The heat transfer equation and the boundary condition equations, including those for the laser action surface and five insulating surfaces, are incorporated into the loss function. This incorporation provides the model with stronger physical constraints on the training data. 2) The locally adaptive activation function method is employed to enhance convergence speed and accuracy.

3.3. TLE-PINN method

The high-fidelity model aligns more closely with experimental results compared to the low-fidelity model (see Section 5.1 for the corresponding conclusions). Notably, low-fidelity data from low-fidelity models converge easily during the training process due to fewer physical equations, whereas high-fidelity data from high-fidelity models present convergence challenges because they encompass more physical equations. To adequately train high-fidelity data, the proposed TLE-PINN method integrates the concepts of DL and PINN methods, as illustrated in Figure 2b. In Step 1, high-fidelity data is used to train the EPINN and update the parameters θ_S, as illustrated on the left side of Figure 2b. In Step 2, the well-trained parameters θ_S except for those in the last layer, are frozen, and the features are preserved. Next, DL training methods are applied to further update the last layer parameters θ_M as illustrated on the right side of Figure 2b. Specifically, physical constraint equations are removed, leaving only the residual equation for the high-fidelity data. The proposed method not only improves training speed but also ensures training accuracy.

4. Experimental setup

4.1. Experimental setup

The SLM system is illustrated in Figure 3a,b and includes a continuous laser, a movable platform, shielding gas, and the sample 42CrMo. First, the sample 42CrMo is fixed on the movable platform. Next, the continuous laser is activated to focus the beam onto the sample surface, inducing melting and subsequent solidification. Simultaneously, the movable platform is moved along the x-axis to cover and process the entire sample surface. The relevant laser parameters, determined through several experiments, are shown in Table 1. This paper presents experiments on laser scanning speeds ranging from 1 mm/s to 9 mm/s.

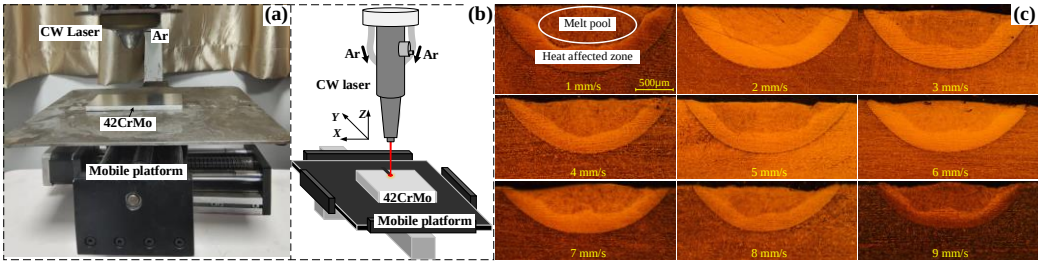

Figure 3. (a),(b) Experimental setup. **(c)** Experimental melt pool morphologies of laser scanning speeds 1–9 mm/s.

4.2. Experimental sample

In this study, 42CrMo steel (30 mm × 24 mm × 3 mm) is used for the experiments. 42CrMo steel is known for its excellent processing and fabrication properties, and its chemical composition is provided in Table 3. To ensure accurate experimental results, the oxide layer and contaminants are removed from the surface of the 42CrMo steel using sandpaper and acetone prior to SLM.

Table 3. Chemical composition of 42CrMo.

Chemical material	Cr	Mo	C	Si	Mn	P	S
Mass percentage (%)	0.92	0.18	0.40	0.30	0.65	0.025	0.025

After SLM, electrical cutting is performed perpendicular to the ablation marks left by the laser on the sample surface. Subsequently, metallographic samples are prepared through mechanical grinding, polishing, and etching. The cross-section of the melt pool and the temperature distribution are subsequently analyzed, as depicted in Figure 3c. The melt pool (innermost layer, with temperatures higher than 1460 K) and the heat-affected zone (sub-innermost layer, with temperatures between 1220 K and 1460 K) are clearly visible [20,29]. As laser scanning speeds increase, both the melt pool size and the heat-affected zone decrease because the area is irradiated for shorter durations, which limits energy accumulation. These results are used to validate the effectiveness of the proposed method in subsequent sections.

5. Results and discussion

5.1. Experiment and simulation results

5.1.1. Effects of high-fidelity model

The comparison between the low-fidelity and high-fidelity models at a laser scanning speed of 1 mm/s is shown in Figure 4. Turbulence-driven enhancements in viscosity and heat conduction improve the model's thermal transfer efficiency, convective effects, and fluid dynamics [30]. These changes subsequently affect temperature distribution and the size of the melt pool. Clearly, the equivalent viscosity coefficient of the high-fidelity model is higher than that of the low-fidelity model (Figure 4a) due to turbulence-induced enhancement. Similarly, the equivalent thermal conductivity of the high-fidelity model is higher than that of the low-fidelity model (Figure 4b) due to turbulence-induced enhancement. Temperature curves at the center of the sample surface and the cross-section for both high-fidelity and low-fidelity models along the laser scanning track are shown in Figure 4c,d. In the region outside the melt pool (temperatures below 1460 K), where turbulence effects are minimal, the temperature profiles of the two models are nearly identical. In the melt pool area (temperatures above 1460 K), where turbulence effects are significant, the low-fidelity model has higher temperature values compared to the high-fidelity model.

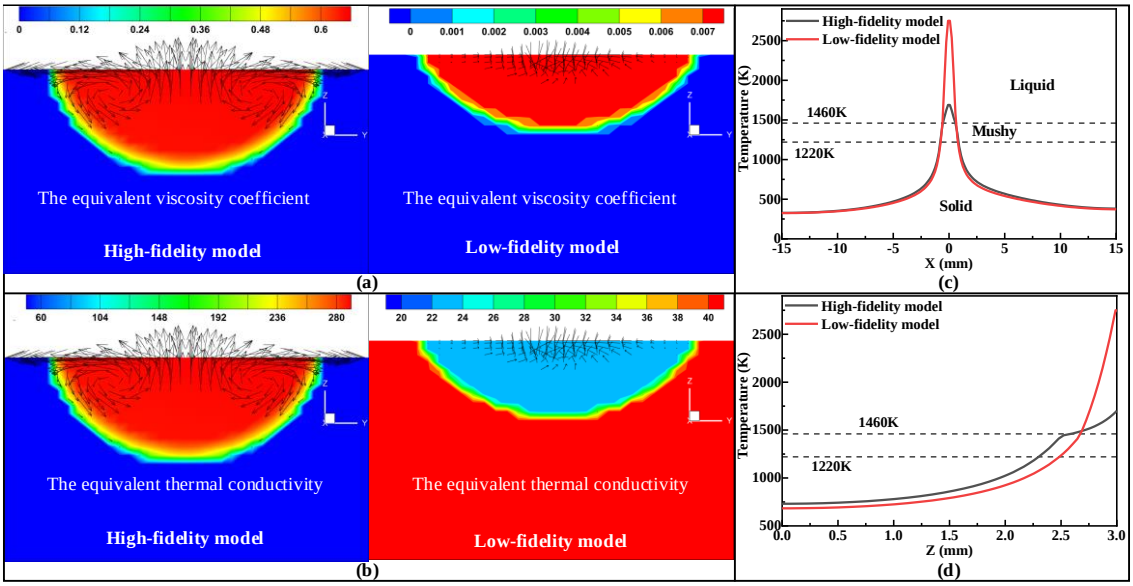

Figure 4. Comparison of high-fidelity model and low-fidelity model. **(a)** Equivalent viscosity coefficient. **(b)** Equivalent thermal conductivity. **(c)** Temperature curves along the sample surface. **(d)** Temperature curves along the sample cross-section.

5.1.2. Comparison of experiment and simulation results

The comparison of low-fidelity and high-fidelity models with experimental results at laser scanning speeds of 1–9 mm/s is shown in Figure 5a,b. Turbulence enhances both heat and mass transfer. Outside the melt pool, the high-fidelity models show higher temperatures than the low-fidelity models at low scanning speeds, where turbulence effects are minimal. In the melt pool area, the high-fidelity models are more consistent with the experimental results compared to the low-fidelity models. The melt pool size (including width and depth) for both models and experiments is shown in Figure 5c. In contrast, the high-fidelity models more accurately match the experimental sizes. Thus, the high-fidelity models are more accurate and consistent with the experimental results.

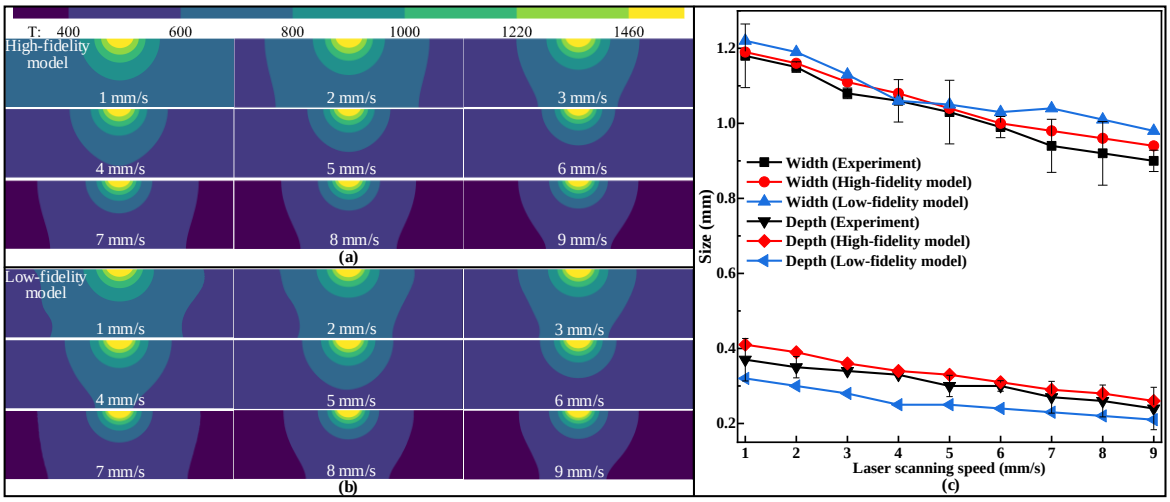

Figure 5. Melt pool morphologies of high-fidelity model and low-fidelity model in laser scanning speeds of 1–9 mm/s. **(a)** High-fidelity model. **(b)** Low-fidelity model. **(c)** Melt pool size for experiment, high-fidelity model, and low-fidelity model.

5.2. Effects of the proposed method

To validate the effectiveness of the proposed method, comparative analyses were conducted using additional methods at laser scanning speeds ranging from 1–9 mm/s, as presented in Table 4.

Table 4. Methods discussed in this paper.

Proposed	1) EPINN with high-fidelity data. 2) DL with high-fidelity data.
PINN/Low-fidelity data	PINN with low-fidelity data
PINN/Unlabeled data	PINN without labeled data

5.2.1. Effects of the transfer learning framework

High-fidelity data from high-fidelity models contains more physical equations, resulting in a slower convergence speed compared to low-fidelity data from low-fidelity models. The convergence speed of the model is critical for determining its real-time performance and efficiency in industrial applications. The loss function curves of the compared methods are illustrated in Figure 6a. The proposed method involves two steps: 1) Training the EPINN model using high-fidelity data, and 2) Freezing the well-trained parameters except for the last layer, after which DL training methods are applied to further update the last layer parameters. In Step 1, the proposed method involves training the EPINN model using high-fidelity data. Clearly, the loss function value of the proposed method decreases more rapidly compared to the traditional PINN model, benefiting from the use of the locally adaptive function as described in Equation (11). This function effectively improves the convergence speed of the model. The PINN model using low-fidelity data converges faster than the model using high-fidelity data because low-fidelity data includes fewer physical equations. In Step 2, the loss function curve of the proposed method decreases significantly because the physical constraint equations are removed from the loss function, leaving only the residual equation for temperature-labeled data to further update the last layer parameters of the EPINN model.

The model size and training time of the above methods are shown in Figure 6b,c. As obviously, the model size and training time of the PINN methods are much lower than those of the high-fidelity model, which demonstrates the superiority of the PINN methods. Particularly, the proposed method has the shortest training time compared to other PINN methods benefiting from the use of the transfer learning framework. To compare the prediction accuracy, the average of the maximum deviation between the predicted results and simulations for laser scanning speeds of 1–9 mm/s is computed and is shown in Figure 6d. In contrast, the proposed method has the lowest deviation, which demonstrates higher predicted accuracy compared to other PINN methods. Thus, the effective combination of DL method and PINN method using the transfer learning framework can significantly improve the training speed and prediction accuracy of the PINN method.

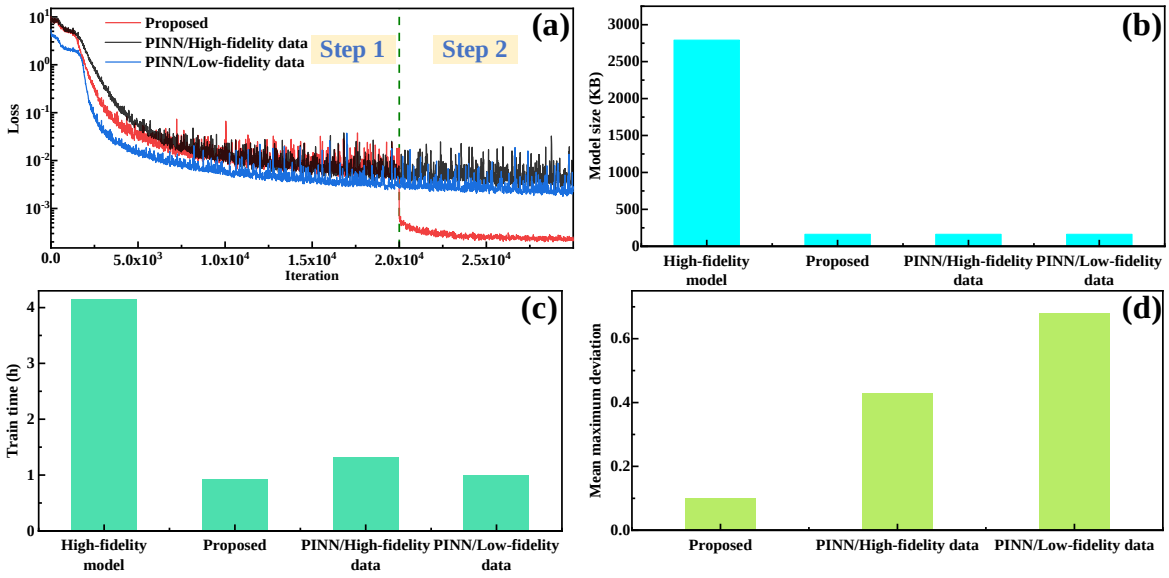

Figure 6. (a) Loss function curves of the compared methods. **(b)** Model size of the compared methods. **(c)** Training time of the compared methods. **(d)** Mean maximum deviation in speeds of 1–9 mm/s of the compared methods.

5.2.2. Comparison with melt pool size

The predicted results of the compared methods are shown in Figure 7. The proposed method employs EPINN to impose strong physical constraints on the data, followed by the application of transfer learning techniques combined with DL methods for further training. This approach improves prediction accuracy, particularly in the melt pool region, which contains complex physical information. The temperature field predicted by the proposed method closely matches that of the high-fidelity model among the compared methods. The PINN/Low-fidelity data method utilizes training data that lacks turbulence effects, leading to a concentrated temperature distribution in the melt pool region. As a result, the temperature field outside the melt pool is lower when compared to the high-fidelity model. The PINN/Unlabeled data method, due to the lack of temperature-labeled data for training, struggles to accurately predict models containing complex physical information.

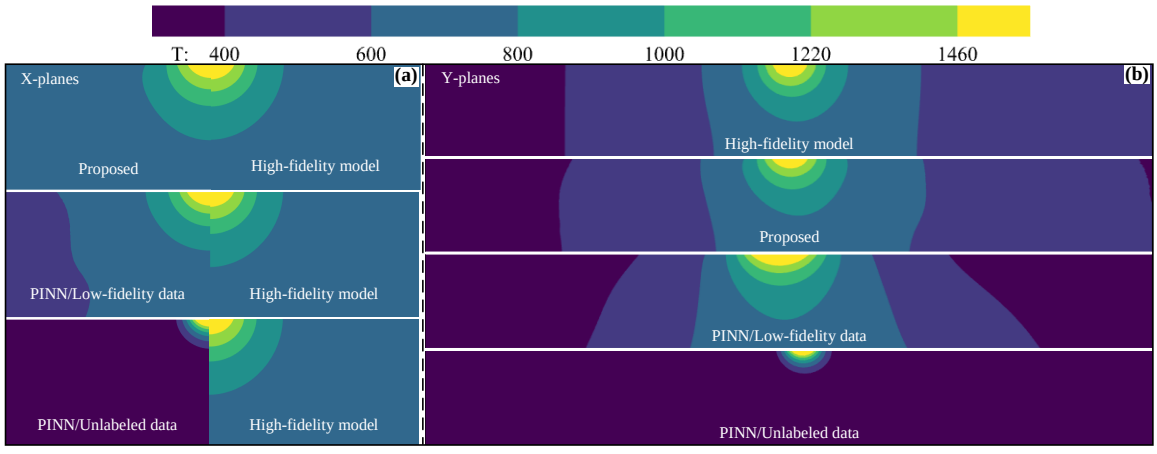

Figure 7. Melt pool morphologies of the compared methods at a laser scanning speed of 1 mm/s in **(a)** X-planes, and **(b)** Y-planes.

The compared methods and experimental results are shown in Figure 8a. In contrast, the melt pool profiles predicted by the proposed method closely match the experimental results. The PINN/Low-fidelity data method exhibits a higher deviation compared to the proposed method and the PINN/High-fidelity data method, which is attributable to reduced accuracy due to the lack of turbulence effects in the training data. The melt pool profile trend predicted by the PINN/Unlabeled data method is similar to the experimental results, but its size deviation is larger. The melt pool size (including width and depth) for the compared methods and experiments at laser scanning speeds of 1–9 mm/s is shown in Figure 8b. The proposed method exhibits the lowest melt pool size deviation in most cases among the compared methods. The PINN/Low-fidelity data method, which utilizes training data without turbulence effects, exhibits a higher deviation compared to the proposed method. The PINN/Unlabeled data method, which solves the simplified heat transfer and boundary condition equations using only temperature-unlabeled data, shows significant size deviations in experimental comparisons.

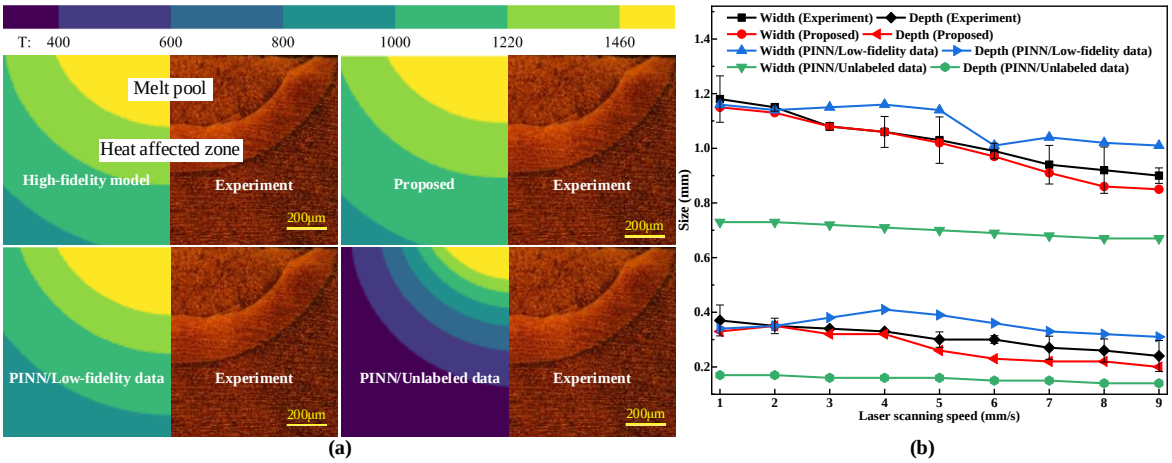

Figure 8. Comparison of the compared methods with experimental results. **(a)** Melt pool morphologies at a laser scanning speed of 1 mm/s. **(b)** Melt pool size at laser scanning speeds of 1–9 mm/s.

5.2.3. Temperature field

The temperature field curves at the center of the sample surface along the laser scanning track for the compared methods and high-fidelity models at laser scanning speeds of 1–9 mm/s are shown in Figure 9. The melting point of 42CrMo is 1460 K. According to the high-fidelity model, the maximum temperature occurs at the center of the melt pool (where x = 0 mm). The temperature gradually decreases as the distance from the melt pool center increases. The PINN/Unlabeled data method, due to the lack of temperature-labeled data for training, struggles to accurately model complex physical systems, resulting in high temperature deviations from the high-fidelity model. In the low-temperature region (temperatures below 1460 K), where turbulence effects are weak, all three methods show good agreement with the high-fidelity model, with slight deviations. However, near the center of the melt pool (x = 0 mm), where turbulence effects are strong, the PINN/Low-fidelity data method, which uses low-fidelity data without turbulence effects, shows high deviation, especially at x = 0. The proposed method, which combines the EPINN model with a transfer learning framework for training high-fidelity data, exhibits the lowest temperature deviation.

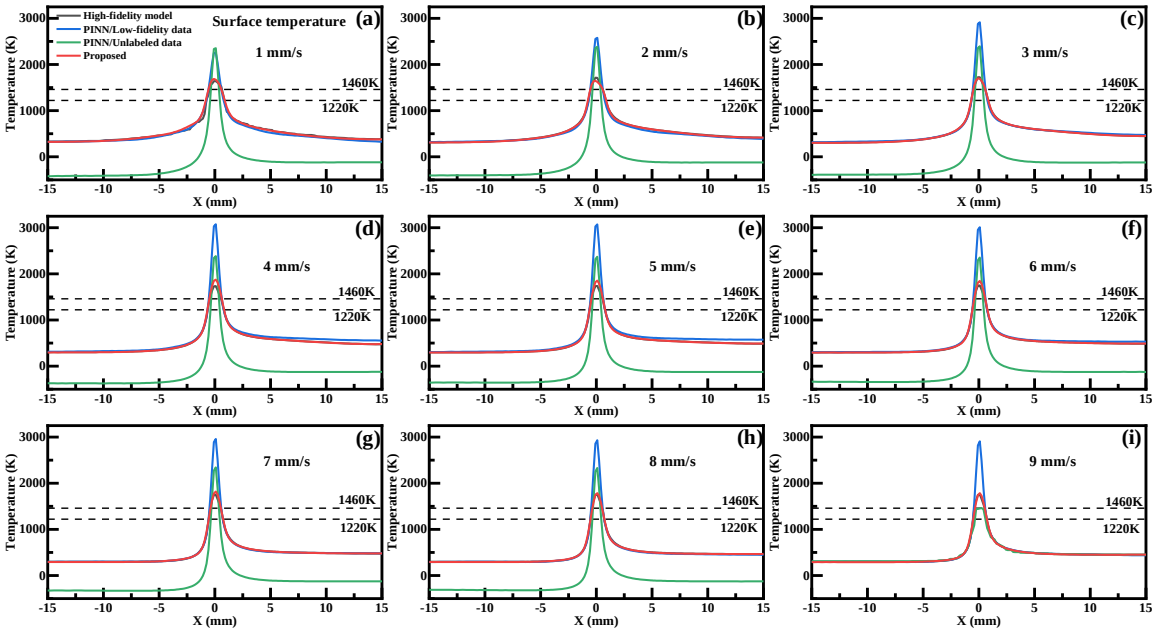

Figure 9. Temperature curves at the center of the sample surface along the laser scanning track of compared methods at speeds of: **(a)** 1 mm/s, **(b)** 2 mm/s, **(c)** 3 mm/s, **(d)** 4 mm/s, **(e)** 5 mm/s, **(f)** 6 mm/s, **(g)** 7 mm/s, **(h)** 8 mm/s, and **(i)** 9 mm/s.

To further validate the prediction accuracy of the compared methods, the temperature deviation T_e between the predicted results and the high-fidelity model is calculated as follows [31]:

$$T_e = \frac{1}{n}\sum_{i=1}^{n}\left|\frac{T_{s,i} - T_{d,i}}{T_{s,i}}\right| \tag{23}$$

in which $T_{s,i}$ is the temperature value of the high-fidelity model at point i. $T_{d,i}$ is the predicted temperature value of the at coordinate point i. n is total number of coordinate points. The average deviation on the sample surface for the compared methods at laser scanning speeds of 1–9 mm/s is shown in Figure 10. The proposed method exhibits the lowest deviation in most cases compared to the compared methods, demonstrating superior performance. The PINN/Low-fidelity data method uses low-fidelity data without turbulence effects, which are strong in the melt pool region. In low-speed cases, the melt pool is larger, resulting in higher deviation. In high-speed cases, the melt pool is smaller, resulting in lower deviation. The PINN/Unlabeled data method shows the highest temperature deviation because it solves the simplified heat transfer equation and boundary conditions using only temperature-unlabeled data.

The temperature gradient along the melt pool depth is crucial, as it significantly impacts the formation of the melt pool. Figure 11 shows the temperature curves at the center of the melt pool cross-section for the compared methods at laser scanning speeds of 1–9 mm/s. The melting point of 42CrMo is 1460 K. The high-fidelity model indicates that the temperature gradually increases from the bottom to the top (z-axis from 0–3 mm) along the center of the sample cross-section, peaking at the center of the melt pool. Similarly, outside the melt pool area (temperatures below 1460 K) where turbulence effects are weak, the temperature curves from the compared methods align with the high-fidelity model, except for the PINN/Unlabeled data method, which struggles with complex physical models, resulting in high deviation. The proposed method shows the lowest temperature deviation compared to the high-fidelity

model among all methods, benefiting from the integration of the EPINN model and transfer learning framework, which effectively trains the high-fidelity data.

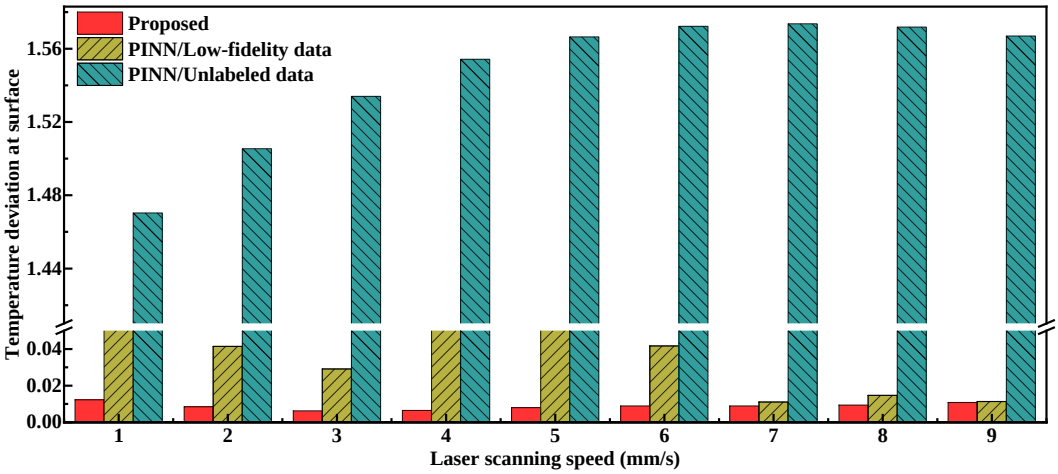

Figure 10. Average temperature deviation on the sample surface for the compared methods at speeds ranging from 1–9 mm/s.

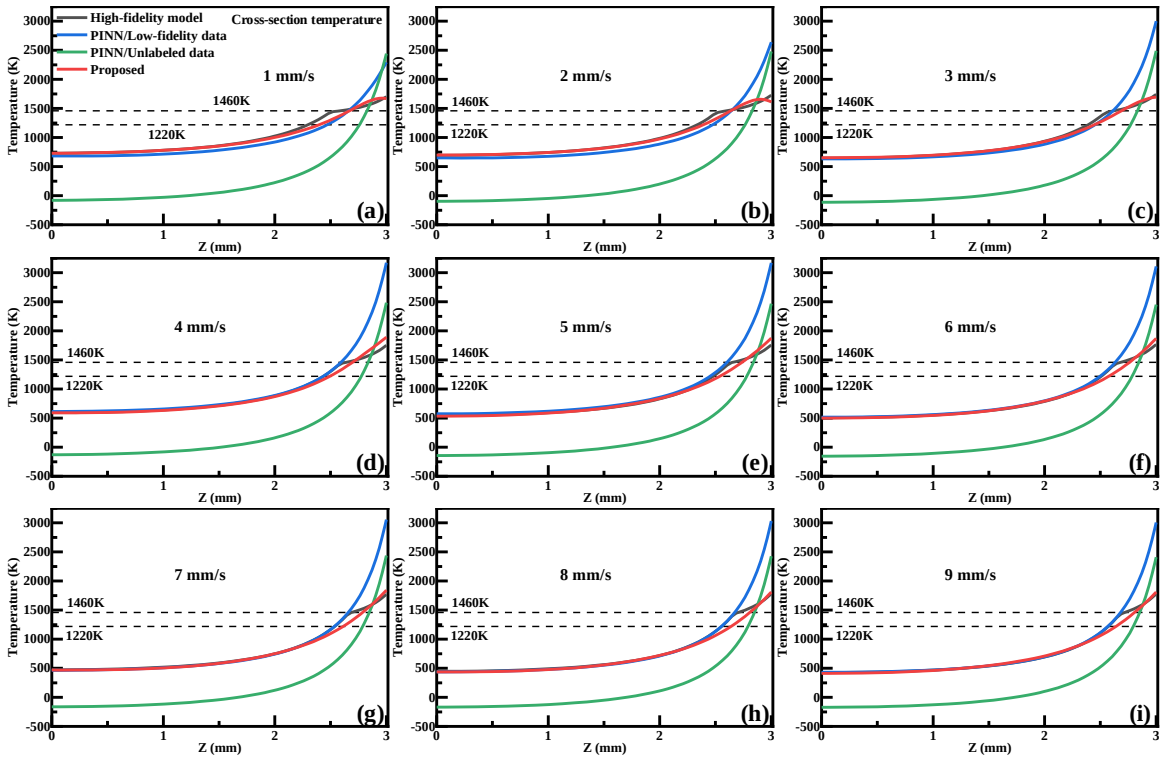

Figure 11. Temperature curves in the center of the melt pool cross-section of compared methods at speeds of: **(a)** 1 mm/s, **(b)** 2 mm/s, **(c)** 3 mm/s, **(d)** 4 mm/s, **(e)** 5 mm/s, **(f)** 6 mm/s, **(g)** 7 mm/s, **(h)** 8 mm/s, and **(i)** 9 mm/s.

Figure 12 shows the average temperature deviation in the sample cross-section for the compared methods at laser scanning speeds of 1–9 mm/s. Similarly, the PINN/Unlabeled data method exhibits the highest deviation because it only solves the simplified heat transfer equation and boundary conditions using temperature-unlabeled data. The PINN/Low-fidelity data method shows higher deviation in low-speed cases, where the melt pool area is larger, and lower deviation in high-speed cases, where the melt

pool area is smaller. The proposed method consistently demonstrates the lowest deviation across most speed cases compared to the other three methods, highlighting its superior performance.

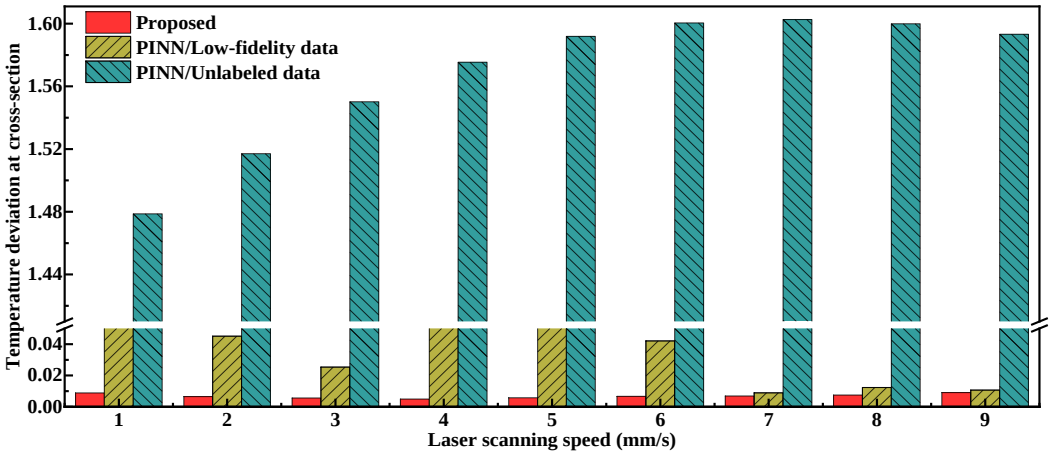

Figure 12. Average temperature deviation in the sample cross-section for the compared methods at speeds of 1–9 mm/s.

5.3. Discussion

5.3.1. Comparison of proposed method with data-driven methods

Data-driven methods are introduced below. Method 1 is Random Forest [32], which integrates multiple decision trees to reduce overfitting and noise. This approach enhances prediction accuracy and reliability, offering significant advantages in advanced manufacturing. Method 2 is XGBoost [33], which combines a gradient boosting algorithm with a decision tree model. This combination allows for prediction using multiple decision trees, thereby optimizing performance. The average temperature deviation on the sample surface and cross-section is calculated according to (18) and shown in Figure 13a,b. The Random Forest and XGBoost methods, being data-driven models without physical constraints, show higher deviation compared to the proposed method when benchmarked against the high-fidelity model. Its performance may be improved by increasing the amount of training data or optimizing the parameters. To ensure comparability, all methods were trained using the same data volume.

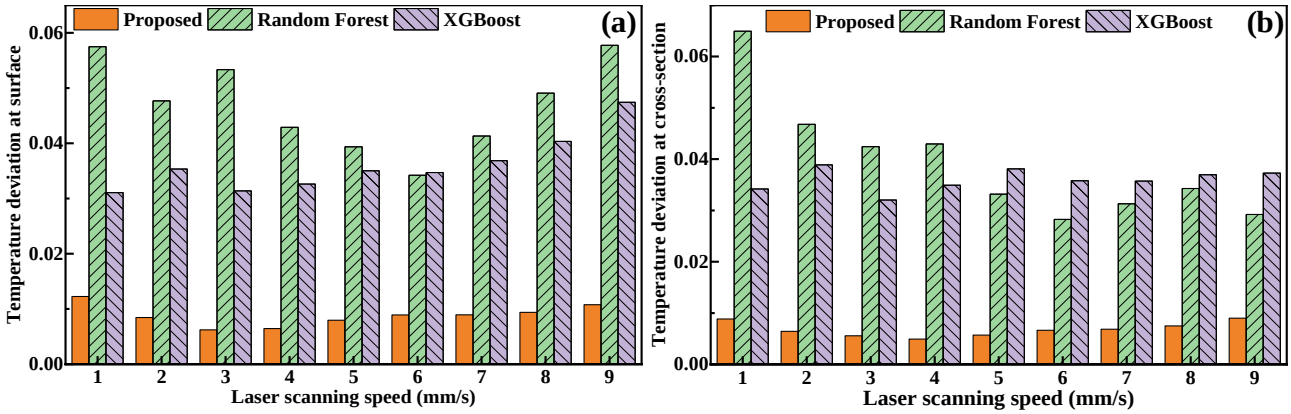

Figure 13. Comparison of the proposed method with data-driven methods. **(a)** Average temperature deviation on the sample surface at laser scanning speeds of 1–9 mm/s. **(b)** Average temperature deviation in the sample cross-section at laser scanning speeds of 1–9 mm/s.

5.3.2. Model robustness

To validate the robustness of the proposed method, all methods are applied using temperature-labeled data for speed cases of 1–5 mm/s, and then used to predict speed cases of 1–9 mm/s. The deviation of the overall sample between these methods and the high-fidelity model are calculated as (18) and is depicted in Figure 14. As shown, the deviation of the proposed method is lower than that of the compared methods. Notably, the proposed method maintains high accuracy in speed cases of 6–9 mm/s, which were not included in the training data, compared to other methods. Therefore, these results demonstrate that the proposed method exhibits superior robustness.

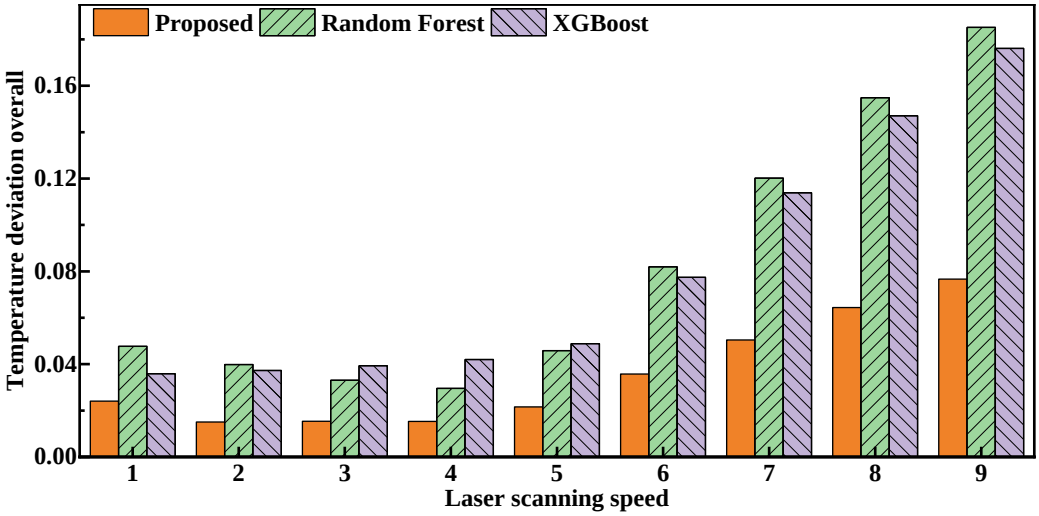

Figure 14. Average temperature deviation in all regions of the sample at speeds of 1–9 mm/s.

5.3.4. Generalizability of transfer learning framework

To validate the effectiveness of the proposed framework, low-fidelity data obtained from the low-fidelity model and high-fidelity data are used in the proposed method, named Proposed_MFD. In the first step, low-fidelity data is used to train the EPINN and update the parameters θ_L, as shown on the left side of Figure 15. In the second step, the well-trained parameters θ_L, except for those in the last layer, are frozen, and the features are preserved. Next, high-fidelity data is used to further train and update the last layer parameters θ_H, as shown on the right side of Figure 15.

The results of the Proposed_MFD method are displayed in Figure 16. The melt pool morphologies of the Proposed_MFD method and the high-fidelity model at a laser scanning speed of 1 mm/s show good agreement in the X-planes (Figure 16a) and Y-planes (Figure 16b). Additionally, the performance of the Proposed_MFD method is further validated by calculating the average temperature deviation from the high-fidelity model on the sample surface and cross-section at laser scanning speeds of 1–9 mm/s, as displayed in Figure 16c,d. The average temperature deviation of the Proposed_MFD method on the sample surface and cross-section is approximately 0.03, which is considered low and acceptable. Therefore, the proposed transfer learning framework has proven effective and can be flexibly applied in industrial applications.

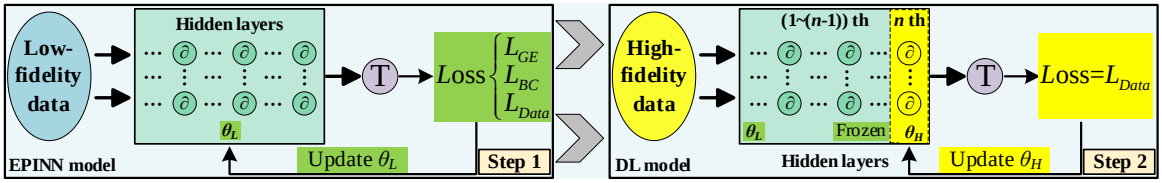

Figure 15. The schematic of a multi-fidelity data transfer learning framework.

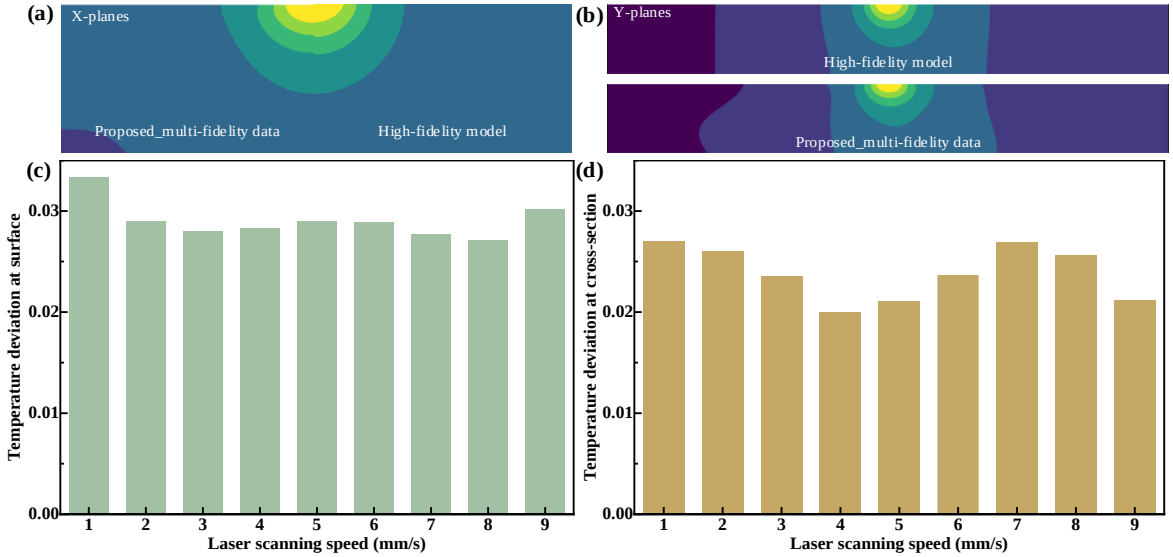

Figure 16. Results of the proposed method with multi-fidelity data. Melt pool morphologies at a speed of 1 mm/s in **(a)** X-planes and **(b)** Y-planes (the maximum temperature deviation is about 0.24, mainly in the area away from the melt pool). **(c)** Average temperature deviation on the sample surface at speeds of 1–9 mm/s. **(d)** Average temperature deviation in the sample cross-section at laser scanning speeds of 1–9 mm/s.

5.3.5. Future work

The proposed method has demonstrated promising results in accurately predicting melt pool morphology and temperature fields through the use of the EPINN model, transfer learning, and high-fidelity model data. Nevertheless, several research directions remain open to further enhance the method's performance and expand its applicability. Given that SLM is a transient, non-equilibrium physicochemical metallurgical process, it poses considerable challenges due to the complex variations in physical fields and the evolution of solid-liquid and gas-liquid interfaces [34]. Although current high-fidelity models offer valuable insights, they are subject to simplifications owing to computational limitations. Future research could aim to refine these models to better capture intricate phenomena, such as phase transitions, heat transfer mechanisms, and microstructural evolution. Emerging methods like attention mechanisms, known for their ability to enhance focus, convergence, and accuracy, present promising opportunities for integration with the EPINN model [35,36]. Currently, the proposed method is applied to the cases for laser scanning speed variations. Future work could investigate the method’s application to other materials or parameters. SLMs with a large combination of parameters will be further investigate to make well predictions. Moreover, with the upgrading and development of computer hardware, the proposed method has great potential for on-line prediction.

6. Conclusion

This article proposes the TLE-PINN method, which combines the PINN model with transfer learning techniques for accurate and efficient prediction in the melt pool size and temperature distribution during the SLM process. First, the EPINN model incorporates heat transfer laws and boundary equations for each surface into the loss function. Additionally, it includes a local adaptive activation function in the training process. The EPINN model demonstrates excellent convergence speed and strong physical constraints on the data. Second, the proposed transfer learning framework integrates physics-informed and data-driven methods for training with high-fidelity data, specifically addressing challenges such as slow or difficult convergence due to the complexity of physical information and limited data accessibility during the SLM process. The effectiveness of the proposed method is validated through comparisons with experimental results, numerical models, and state-of-the-art methods, including PINN and DL techniques. The comparison results demonstrate that the proposed method exhibits superior performance across various aspects, showing significant potential for industrial applications.

Acknowledgments

This work was supported by the Science and Technology program of Wuhan City (Grant No. 2024071104010833), and the National Natural Science Foundation of China (Grant No. 51901162). The authors acknowledge the support of the National Talent Program of China.

Conflicts of interests

The authors declare that they have no known competing financial interests or personal relationships that could have appeared to influence the work reported in this paper.

Authors' contributions

Conceptualization, Qingyun Zhu and Yaowu Hu; methodology, Qingyun Zhu and Yaowu Hu; software, Zhengxin Lu; validation, Yaowu Hu, Qingyun Zhu and Zhengxin Lu; formal analysis, Qingyun Zhu; investigation, Qingyun Zhu; resources, Yaowu Hu; data curation, Qingyun Zhu; writing—original draft preparation, Qingyun Zhu; writing—review and editing, Yaowu Hu; visualization, Qingyun Zhu; supervision, Yaowu Hu; project administration, Yaowu Hu; funding acquisition, Yaowu Hu. All authors have read and agreed to the published version of the manuscript.

Data Availability

Data will be made available on request.

Reference

[1] Bin C, Wang F, Ren S, Xia P, Wang Z, *et al.* Influence of erbium addition on microstructure and performances of AlSi10Mg alloy prepared by selective laser melting. *J. Rare Earths* 2023, 42(10):1817–2002.

[2] Wang M, Gao J, Zhang L, Song B. A new AlSi7Mg-xSc alloy with high strength and high strain Manufactured by Selective Laser Melting. *J. Mater. Res. Technol.* 2024, 30:4272–4282.

[3] Akbari P, Ogoke F, Kao NY, Meidani K, Yeh CY, *et al.* MeltpoolNet: Melt pool characteristic prediction in Metal Additive Manufacturing using machine learning. *Addit. Manuf.* 2022, 55:1–17.
[4] Cheng Y, Wang G, Qiu Z, Zheng Z, Zeng D, *et al.* Multi-physics simulation of non-equilibrium solidification in Ti-Nb alloy during selective laser melting. *Acta Mater.* 2024, 272:119923.
[5] Gu H, Wei C, Li L, Han Q, Setchi R, *et al.* Multi-physics modelling of molten pool development and track formation in multi-track, multi-layer and multi-material selective laser melting. *Int. J. Heat Mass Transfer* 2020, 151:119458.
[6] Jiang P, Gao S, Geng S, Han C, Mi G. Multi-physics multi-scale simulation of the solidification process in the molten pool during laser welding of aluminum alloys. *Int. J. Heat Mass Transfer* 2020, 161:120316.
[7] Xia Q, Sun G, Kim J, Li Y. Multi-scale modeling and simulation of additive manufacturing based on fused deposition technique. *Phys. Fluids* 2023, 35(3):034116.
[8] Kiangala SK, Wang Z. An effective adaptive customization framework for small manufacturing plants using extreme gradient boosting-XGBoost and random forest ensemble learning algorithms in an Industry 4.0 environment. *Mach. Learn. Appl.* 2021, 4:100024–100024.
[9] Lu J, An K, Wang X, Song J, Xie F, *et al.* Compressed Channel-Based Edge Computing for Online Motor Fault Diagnosis With Privacy Protection. *IEEE Trans. Instrum. Meas.* 2023, 72:1–12.
[10] Ferrer-Sánchez A, Martín-Guerrero JD, de Austri-Bazan RR, Torres-Forné A, Font JA. Gradient-annihilated PINNs for solving Riemann problems: Application to relativistic hydrodynamics. *Comput. Methods Appl. Mech. Eng.* 2024, 424:116906.
[11] Huang AJ, Agarwal S. Physics-Informed Deep Learning for Traffic State Estimation: Illustrations with LWR and CTM Models. *IEEE Open J. Intell. Transp. Syst.* 2022, 3:503–518.
[12] Guo S, Agarwal M, Cooper C, Tian Q, Gao RX, *et al.* Machine learning for metal additive manufacturing: Towards a physics-informed data-driven paradigm. *J. Manuf. Syst.* 2022, 62145–163.
[13]Hu H, Qi L, Chao X. Physics-informed Neural Networks (PINN) for computational solid mechanics: Numerical frameworks and applications. *Thin-Walled Struct.* 2024:112495.
[14] Vu-Quoc L, Humer A. Deep Learning Applied to Computational Mechanics: A Comprehensive Review, State of the Art, and the Classics. *CMES-Comp. Model. Eng. Sci.* 2023, 137(2):1070–1343.
[15] Koric S, Abueidda DW. Data-driven and physics-informed deep learning operators for solution of heat conduction equation with parametric heat source. *Int. J. Heat Mass Transfer* 2023, 203:123809.
[16] Li S, Wang G, Di Y, Wang L, Wang H, *et al.* A physics-informed neural network framework to predict 3D temperature field without labeled data in process of laser metal deposition. *Eng. Appl. Artif. Intell.* 2023, 120:105908.
[17] Wang H, Li B, Xuan FZ. A dimensionally augmented and physics-informed machine learning for quality prediction of additively manufactured high-entropy alloy. *J. Mater. Process. Technol.* 2022, 307:117637.
[18] Hosseini E, Gh Ghanbari P, Müller O, Molinaro R, Mishra S. Single-track thermal analysis of laser powder bed fusion process: Parametric solution through physics-informed neural networks. *Comput. Methods Appl. Mech. Eng.* 2023, 410:116019.
[19] Jagtap AD, Kawaguchi K, Karniadakis GE. Adaptive activation functions accelerate convergence in deep and physics-informed neural networks. *J. Comput. Phys.* 2020, 404:109136.
[20] Jiang F, Xia M, Hu Y. Physics-Informed Machine Learning for Accurate Prediction of Temperature and Melt Pool Dimension in Metal Additive Manufacturing. *3D Print. Addit. Manuf.* 2023, 11(4):1407–1417.
[21] Zhu Q, Lu Z, Hu Y. A reality-augmented adaptive physics informed machine learning method for efficient heat transfer prediction in laser melting. *J. Manuf. Processes* 2024, 124:444–457.
[22] Srilakshmi V, Kiran GU, Mounika M, Sravanthi A, Sravya NVK, *et al.* Evolving Convolutional Neural Networks with Meta-Heuristics for Transfer Learning in Computer Vision. *Procedia Comput. Sci.* 2023, 230:658–668.
[23] Shao H, Li W, Xia M, Zhang Y, Shen C, *et al.* Fault Diagnosis of a Rotor-Bearing System under Variable Rotating Speeds Using Two-Stage Parameter Transfer and Infrared Thermal Images. *IEEE Trans. Instrum. Meas.* 2021, 70:1–11

[24] Chou JS, Chong PL, Liu CY. Deep learning-based chatbot by natural language processing for supportive risk management in river dredging projects. *Eng. Appl. Artif. Intell.* 2024, 131:107744.
[25] Chakraborty S. Transfer learning based multi-fidelity physics informed deep neural network. *J. Comput. Phys.* 2021, 426:109942.
[26] Hu Y, He X, Yu G, Ge Z, Zheng C, *et al.* Heat and mass transfer in laser dissimilar welding of stainless steel and nickel. *Appl. Surf. Sci.* 2012, 258(15):5914–5922.
[27] Baydin AG, Pearlmutter BA, Radul AA, Siskind JM. Automatic Differentiation in Machine Learning: a Survey. *J. Mach. Learn. Res.* 2018, 18(153):1−43.
[28] Pu J-C, Chen Y. Data-driven forward-inverse problems for Yajima–Oikawa system using deep learning with parameter regularization. *Commun. Nonlinear Sci. Numer. Simul.* 2023, 118:107051.
[29] Zhao S, Yu G, He X, Zhang Y, Ning W. Numerical simulation and experimental investigation of laser overlap welding of Ti6Al4V and 42CrMo. *J. Mater. Process. Technol.* 2011, 211(3):530–537.
[30] Khairallah SA, Chin EB, Juhasz MJ, Dayton AL, Capps A, *et al.* High fidelity model of directed energy deposition: Laser-powder-melt pool interaction and effect of laser beam profile on solidification microstructure. *Addit. Manuf.* 2023, 73:103684.
[31] Tang H, Liao Y, Yang H, Xie L. A transfer learning-physics informed neural network (TL-PINN) for vortex-induced vibration. *Ocean Eng.* 2022, 266:113101.
[32] Behnke M, Guo S, Guo W. Comparison of early stopping neural network and random forest for in-situ quality prediction in laser based additive manufacturing. *Procedia Manuf.* 2021, 53:656–663.
[33] Xie J, Li Z, Zhou Z, Liu S. A Novel Bearing Fault Classification Method Based on XGBoost: The Fusion of Deep Learning-Based Features and Empirical Features. *IEEE Trans. Instrum. Meas.* 2021, 70:1–9.
[34] Anand N, Chang KC, Yeh AC, Chen YB, Lee MT. Development of a comprehensive model for predicting melt pool characteristics with dissimilar materials in selective laser melting processes. *J. Mater. Process. Technol.* 2023, 319:118069.
[35] Anagnostopoulos SJ, Toscano JD, Stergiopulos N, Karniadakis GE. Residual-based attention in physics-informed neural networks. *Comput. Methods Appl. Mech. Eng.* 2024, 421:116805.
[36] Ayetiran EF, Özgöbek Ö. An inter-modal attention-based deep learning framework using unified modality for multimodal fake news, hate speech and offensive language detection. *Inf. Syst.* 2024:102378–102378.